

Infrared spectra of methane-containing ice mixtures for JWST data analysis

V. Karteyeva, R. Nakibov, I. Petrushkevich, M. Medvedev, and A. Vasyunin

Research Laboratory for Astrochemistry, Ural Federal University, Kuibysheva St. 48, Yekaterinburg 620026, Russia
e-mail: varvara.karteeva@urfu.ru

Received

ABSTRACT

Context. Solid methane (CH_4) is an important molecule in interstellar and planetary environments, serving as a precursor to complex organic compounds and a potential biosignature in exoplanetary studies. Despite its significance, laboratory data on low-temperature phase of methane below 10 K remain limited.

Aims. We aim to obtain spectra of methane in binary mixtures at 10 K and compare it to the spectra obtained at 6.7 K. These temperatures correspond to phases II and II* of pure methane and are representative of dark molecular clouds and protostars at early stages. We also aim to test the obtained data applicability to JWST data interpretation.

Methods. Laboratory reference spectra were obtained on the ISEAge setup via FTIR spectroscopy in transmission mode. A weighted χ^2 minimization is used for the fitting.

Results. We present infrared spectra with corresponding band strengths of pure methane and binary mixtures with methane: $\text{CH}_4:\text{H}_2\text{O}$, $\text{CH}_4:\text{CO}_2$, $\text{CH}_4:\text{CH}_3\text{OH}$, $\text{CH}_4:\text{NH}_3$ at 6.7 K and 10 K showing a 20% increase in mixtures compared to commonly used 10 K band strength value of pure methane. We also test the usability of the spectra on open JWST data by probing the spatial distribution of methane in B335. We also present additional experiments concerning the phase transition of methane between phase II* and phase II.

Conclusions. Our results reveal distinct spectral features for methane in non- H_2O environments, enabling more accurate interpretation of JWST observations. The dataset of spectra, publicly available on Zenodo, can be used for fitting JWST data.

Key words. Astrochemistry, Methods: laboratory: solid state, Stars: protostars, ISM: abundances, ISM: molecules, Infrared: ISM

1. Introduction

Solid methane is the most abundant and one of the simplest hydrocarbon molecules found in prestellar objects and protostars (Öberg et al. 2008). Both theoretical (Hassel et al. 2008; Harada & Herbst 2008; Carder et al. 2021) and experimental (Baratta et al. 2002; Hodyss et al. 2009; Abplanalp et al. 2018; Zhu et al. 2018) studies consider methane a precursor for more complex carbonaceous molecules. Also, it can possibly be considered as a biosignature for exoplanetary studies (Krissansen-Totton et al. 2018; Thompson et al. 2022; Glass & Hörlst 2025). Methane is a part of the atmosphere of planets, e.g. Jupiter and Mars (Gautier et al. 1982; Krasnopolsky et al. 2004) and exoplanets, e.g. HD 209458b and HR 8799 b (Swain et al. 2009; Barman et al. 2015).

The first discovery of interstellar solid methane occurred by the ground-based infrared echelle spectrograph (IRSHELL) (Lacy et al. 1991). Methane is usually identified on infrared (IR) spectra using $7.7\ \mu\text{m}$ ($\sim 1300\ \text{cm}^{-1}$) deformation mode absorbance band. Boogert et al. (1996) performed the first fit of methane absorption band at $7.7\ \mu\text{m}$ with $\text{CH}_4:\text{H}_2\text{O}$ ice spectrum and proposed the $\text{CH}_4:\text{CH}_3\text{OH}$ and $\text{CH}_4:\text{NH}_3$ mixtures as alternatives. Based on shape and position of absorbance band it was concluded that methane is contained within the polar layer of ice mantles on interstellar dust (Boogert et al. 1998). Methane was identified in a number of objects in Infrared Space Observatory (ISO) data review (Gibb et al. 2004), where spectra of pure methane and methane in mixture with H_2O were used. Later, methane abundance was constrained using Spitzer data,

where methane was fitted with $\text{CH}_4:\text{H}_2\text{O}$ mixtures (Öberg et al. 2008). Currently, research on methane continues with the recent *James Webb* Space Telescope (JWST) data. The deformation mode of solid methane at $7.7\ \mu\text{m}$ is described by methane-bearing H_2O ices: at 15 K ($\text{H}_2\text{O}:\text{CH}_4 = 10:1$ ¹, Rocha et al. 2024) in IRAS 2A and IRAS 23385+6053, at 13 K ($\text{H}_2\text{O}:\text{CH}_4 = 100:6$, Chen et al. 2024) in B1-c, at 12 K ($\text{H}_2\text{O}:\text{CH}_4 = 10:1$, Rocha et al. 2025) in Ced 110 IRS4, H_2O and CO_2 environment at 12 K² ($\text{H}_2\text{O}:\text{CO}_2:\text{CH}_4 = 10:1:1$, McClure et al. 2023) in NIR38 and J110621, using a complex mixture at 10 K ($\text{H}_2\text{O}:\text{CH}_3\text{OH}:\text{CO}_2:\text{CH}_4 = 0.6:0.7:1:0.1$, Yang et al. 2022) in IRAS 15398–3359 and $\text{H}_2\text{O}:\text{CH}_4 = 10:1$ at ~ 8 K and $\text{CO}_2:\text{CH}_4 = 5:1$ at ~ 27 K (Nakibov et al. 2025) in IRAS 23385+6053. According to these findings on JWST data the methane abundance in cold clouds and star-forming regions is 1.6–3.7% with respect to solid H_2O .

There are three phases of solid methane under vacuum conditions: phase I is stable above 20.4 K, phase II — below 20.4 K (e.g. Gerakines & Hudson 2015b), and the third phase, stable if methane is deposited below 10 K (Colwell et al. 1962; Krupskii et al. 1973; Emtiaz et al. 2020). Following Emtiaz et al. (2020) we refer to this third phase as crystalline phase II*. However, the literature spectra of methane typically used for interpretation of observational data are obtained at a

¹ Mixtures used in fitting procedures in the cited work are shown with this notation

² Note that the spectrum that is referred to in fitting procedure is not listed in the original paper (Rocha et al. 2017)

temperature of 10 K and above, and the laboratory data on ice analogues are present as water-based mixtures for phases I and II (Hudson & Moore 1999; Ehrenfreund et al. 1999; Rocha et al. 2017; Mifsud et al. 2023). Binary mixtures of methane with H_2O , CO , CH_3OH , NH_3 , CO_2 , N_2 , O_2 for the first time were described in Boogert et al. (1997) at 10 K yet the spectral data needed for fitting is unavailable. There are also reflection-mode studies (e.g. Kaiser et al. 2014; Maity et al. 2014; Förstel et al. 2017; Bergantini et al. 2018) that characterize methane photochemistry using relevant laboratory ices, however, their spectra are not directly comparable to astronomical observations of ices in transmission.

In this paper we present laboratory spectra of binary methane-containing ices in transmission regime, that are currently missing in the literature. These mixtures correspond to the environment of the polar layer of ice on the dust grains and aimed for interpretation of JWST data. The ices have astrochemically relevant component ratios: $\text{CH}_4:\text{H}_2\text{O} = 1:10$, $\text{CH}_4:\text{CO}_2 = 1:5$ and $1:15$, $\text{CH}_4:\text{CH}_3\text{OH} = 1:3$, $\text{CH}_4:\text{NH}_3 = 1:3$. The set of mixtures is obtained at a substrate temperature of 10 K. However, in cold prestellar cores temperature may reach as low as 6 K, which is confirmed by, e.g. observations of gas and dust in centres of isolated cold dense cores L183 and L1544 (Pagani et al. 2004, 2007; Crapsi et al. 2007; Pagani et al. 2015). Also, physical modeling of L1544 resulted in the dust temperature in the core center equal to 6.5 K (Keto & Caselli 2010). The presence of dust colder than 10 K is also confirmed by observations obtained with SCUBA at $850\text{ }\mu\text{m}$ (Evans et al. 2001; Pattle et al. 2015). Therefore the set was extended with ices grown at 6.7 K with same composition. The extended set explores the difference between the ices grown at 6.7 K and 10 K substrate temperatures, which correspond to crystalline II* and crystalline II phases of pure methane. The transmission spectra of methane in binary mixtures grown at 6.7 K and $\text{CH}_4:\text{CH}_3\text{OH}$, $\text{CH}_4:\text{NH}_3$ at 10 K are presented here for the first time. The band strengths of methane in various environment are provided as well.

In our previous paper (Nakibov et al. 2025) we described gaseous and solid methane in IRAS 23385+6053 using some of the spectra presented here. In this paper we show the utility of our new infrared spectra by exploring the spatial distribution of methane in JWST spectra of the variable protostar B335-IRS (hereafter B335). B335 is an isolated nebula at a distance of 90–120 pc with a young class 0 protostar IRAS19347+0727 (age $\sim 10^4$ yr, Yıldız et al. 2015). It is associated with protostellar high-velocity Herbig-Haro (HH) jet (Reipurth et al. 1992; Gálfalk & Olofsson 2007). This source has a high level of accretion and two outflows (Bjerkeli et al. 2019) and had a luminosity increase by a factor of 5–7 (Evans et al. 2023). This source is a natural laboratory to study ice chemistry at the early stages of star formation. While the sublimation of complex ices and the rich gas-phase chemistry near the heated core was observed at millimeter wavelengths (Lee et al. 2025), we focus here on the solid methane features at $7.7\text{ }\mu\text{m}$ located within the outflow cavity wall. This allows us to probe the composition of ices in the cold envelope of a young protostar.

2. Experimental methods

All experiments on growing analogues of interstellar ice were carried out on Ice Spectroscopy Experimental Aggregate (ISEAge) that utilizes ultra-high vacuum setup. A detailed description of our installation is provided in Ozhiganov et al. (2024). Briefly, the molecules are deposited on the Ge substrate

from two sides via ‘background deposition’. The 6 mm diameter circle area ($S=0.28\text{ cm}^2$) of the window is available for the deposition of the ice. The substrate is mounted on a cryogenic finger of a closed cycle He cryostat, and the whole chamber is continuously evacuated to the base pressure of $2\times 10^{-10}\text{ mbar}$. The operating temperatures are within the 6.7–305 K range with an error <0.1 K. The setup is equipped with a Stanford Research Systems RGA200 quadrupole mass spectrometer and Thermo Scientific Nicolet iS50 Fourier Transform Infrared (FTIR) spectrometer operating within a $4000\text{--}630\text{ cm}^{-1}$ ($2.5\text{--}15.9\text{ }\mu\text{m}$) with 1 cm^{-1} resolution. The points in the collected spectra are spaced at 0.12 cm^{-1} intervals due to the Zero Filling performed on the interferometer level. The infrared spectra are collected in transmission regime. The FTIR spectrometer and optical path outside the main chamber are flushed by pure N_2 . Gaseous species are introduced into the main chamber via two independent leak valves.

We followed the same experimental procedure for growing of all ices. The component ratio was controlled during the deposition by means of the quadrupole mass spectrometer (QMS). In all experiments both components of a binary mixture were deposited simultaneously. The first component introduced into the main chamber was the pure methane and the second component was a matrix molecule introduced shortly after the desired ion current of methane was reached. The mixture deposition time started when ion currents for both components reached the desired values. This approach allows to correct the influence of ion interference and overlapping ion currents, and maintain the same ion current for methane across all the experiments. The ion current values were taken from the calibration curves obtained for our setup via the procedure similar to Slavicinska et al. (2023). Briefly, the rate at which gaseous molecules are adsorbed on the substrate depends nonlinearly on the ion current and is unique to each molecule. By growing pure ices at different ion currents we can obtain this dependency via experiment allowing for a more precise control over the components ratio of mixed ices. The rates for the calibration curves are determined by measuring the absorbance on the IR spectrum output using the literature band strength values. Since the depositions were conducted on the Ge substrate cooled to 10 K and 6.7 K we used the band strength for methane in phase II (corrected for density) from Bouilloud et al. (2015) and for methane in phase II* from Gerakines & Hudson (2015b), correspondingly.

For both sets of experiments the methane deposition rate was fixed at $5.9 \times 10^{12}\text{ cm}^{-2}\text{ s}^{-1}$ and the second component deposition rate varied based on the desired components ratio. Deposition continued for 120 minutes. Thus, we get a column density of $4.25 \times 10^{16}\text{ cm}^{-2}$ for CH_4 . This approach enables the comparison of methane deformation (1300 cm^{-1}) and stretching (3000 cm^{-1}) modes in various molecular environment. The IR spectra were recorded every 45 seconds (an average of 32 scans). For the analysis in each experiment the last recorded spectrum of deposition was used to avoid the secondary adsorption effect after closing the leak valve. This effect is present when working with volatile species such as CH_4 , CO or N_2 both in static conditions and during the warm up, see Appendix A for details. For calculations of peak positions and areas spectra are baseline-corrected for overall slope and local thin-film interference artifacts. Repeated measurements (50 iterations) with randomized local baseline adjustments are analyzed to minimize noise effects. The final values are derived from the averaged results.

The compounds used are as follows: CH_4 (99.999 %, Ugra-PGS), CO_2 (99.9999 %, Ugra-PGS), NH_3 (99.9 %, UralKri-oGaz), deionized H_2O , CH_3OH (≥ 99.8 %, Vekton). Gaseous

CO_2 and CH_4 are introduced directly into the dosing lines from the commercially acquired gas bottles. H_2O , NH_3 and CH_3OH were purified by a freeze-pump-thaw cycle three times before each experiment. Before each deposition every compound is checked for purity by means of mass-spectrometry.

3. Results

3.1. Binary mixtures with CH_4

In this section we present a series of experiments on obtaining the binary ices of methane with molecules that constitute the polar layer of the interstellar ice mantles. We obtained binary mixtures at a temperature of 10 K, with methane molecules embedded in a matrix of H_2O , CO_2 , CH_3OH or NH_3 . The component ratio was chosen to qualitatively reflect current astrochemical view on species abundances in interstellar ices in cold dense molecular clouds (Boogert et al. 2015; Goto et al. 2021; McClure et al. 2023; Jiménez-Serra et al. 2025). Additionally, the comparative set was obtained at the minimum stable temperature of the ISEAge setup at 6.7 K. Methane absorption bands in mixtures at 6.7 K spectra differ both from pure methane and 10 K mixtures features. We present the spectra of mixtures for both temperatures in Fig. 1. Additional experiments concerning pure methane and its transition between phases II* and II are presented in Appendix A. The methane absorption bands change shape and position in mixed ices, the components ratio and peak position of 3000 cm^{-1} stretching and 1300 cm^{-1} deformation mode are presented in Table 1. The band strengths for the deformation mode of methane in various mixtures are also included. Methane deformation mode in $\text{CH}_4:\text{CO}_2 = 1:5$ mixture stands out because of its structure. It displays an unresolved double peak both in 6.7 K and 10 K experiments, which becomes resolved on heating after 30–40 K (Boogert et al. 1997; Nakibov et al. 2025). Moreover, this mixture displays the most distinction between the two temperatures in both vibrational modes. This is caused by pure CO_2 having an amorphous and crystalline form as shown in Gerakines & Hudson (2015a). For our fixed column density of $2.12 \times 10^{17} \text{ cm}^{-2}$ pure CO_2 fully crystallizes at 10 K and only partially at 6.7 K. An addition of methane, however, prevents CO_2 from crystallizing at 6.7 K. To further investigate this we obtained more diluted mixtures: $\text{CH}_4:\text{CO}_2 = 1:15$ at 6.7 K and 10 K, the differences persisted despite the higher CO_2 concentration. We report, therefore, the peak shape of methane differs significantly in crystalline and amorphous CO_2 . We also note that the double peak gets resolved at 10 K in $\text{CH}_4:\text{CO}_2 = 1:15$ mixture, which is in line with Hudgins et al. (1993), where the double structure is observed in $\text{CH}_4:\text{CO}_2 = 1:20$ mixture at 10 K.

Methane mixtures with CH_3OH and NH_3 show similar features in 1300 cm^{-1} region and have close band strengths values. The features are redshifted by 2 cm^{-1} from the $\text{H}_2\text{O}:\text{CH}_4$ feature. This opens a possibility of singling out methane not related to water ice in observational spectra, an idea first introduced by Boogert et al. (1996). This is important, as normally methane is assumed to be formed simultaneously with water and ammonia ice via hydrogenation of carbon atoms at the onset of the formation of icy grain mantles (Qasim et al. 2020; Lamberts et al. 2022; Ferrero et al. 2023). However, methane can also be formed as a product of photoprocessing or ion-bombardment of methanol-rich ices (Islam et al. 2014) at later stages of ice evolution or via electron-induced radiolysis (Sullivan et al. 2016). The presented data allows potentially to explore the relative importance of both scenarios of methane formation.

3.2. B335 methane survey

To test the usability of the obtained spectra we fitted the $7.7 \mu\text{m}$ methane absorption band of the Class 0 protostar B335. JWST Mid-IR Instrument (MIRI) Medium Resolution Spectrograph (MRS) observations toward B335 are provided within the Investigating Protostellar Accretion proposal (PID 1802, P.I. T. Megeath; Megeath et al. 2021). Level 3 observation data were taken from the MAST database (MAST DOI: 10.17909/yr06-tf19), we further scaled the CH2-SHORT channel data to match the CH1-LONG signal level. MIRI MRS observations included three levels of JWST calibration pipeline with version 1.19.1 and Calibration References Data System (CRDS) context jwst_1413.pmap (CRDS_VER = '12.1.11') describing in Greenfield & Miller (2016); Bushouse et al. (2024); van Gelder et al. (2024). Unfortunately, the overlap region coincides with the OCN^- absorption band and we excluded this species from the further analysis.

B335 is viewed edge-on and has two prominent outflows (e.g. Bjerkeli et al. 2019), the west of which displaying strong continuum emission around $7.7 \mu\text{m}$. Based on the intensity map at $8 \mu\text{m}$ (Fig. 2) we picked multiple apertures that cover bright pixels. This approach maximizes the signal-to-noise ratio, enhancing the analysis of the finer spectral details. To date, this is the first study that explores the spatial distribution on MIRI-MRS JWST data for a molecule with relatively low abundance relative to H_2O . We note that a spatial distribution study was carried out recently for solid H_2O , CO and CO_2 on the NIR-Cam data (Smith et al. 2025). The spectra were extracted from the cylindrical apertures: seven $1.53''$ apertures were used to assess the spatial distribution of methane and a $4.59''$ aperture was used to ensure consistency between fits in smaller apertures. The center positions for the chosen apertures are listed in Table 2.

All spectra were processed in the same way. After baseline subtraction a linear combination of methane laboratory mixtures was fitted to the observational spectrum. The linear scale coefficients were obtained by minimizing χ^2 , given as:

$$\chi^2 = \sum_{i=1}^{N_{\text{obs}}} \frac{(\tau_{\text{obs}}^i - \tau_{\text{model}}^i)^2}{\sigma_i^2}, \quad (1)$$

where τ_{obs} and τ_{model} are observational and modeled optical depths, respectively, and σ_i is the point-wise standard deviation of the observational spectrum. The standard deviation was obtained from the residuals between the original optical depth spectrum and a smoothed curve obtained with locally weighted scatterplot smoothing (LOWESS, Cleveland 1979) with a 24-point window. Column densities of H_2O and CO_2 were estimated based on $6 \mu\text{m}$ and $15.2 \mu\text{m}$ bands, respectively.

The fitted spectra are shown in the Fig. 3. The *a-g* observational spectra correspond to the *a-g* apertures from Fig. 2. Fitting results show that about 70% and 30% of methane budget in B335 are best described by methane in H_2O and methane in CO_2 environments, respectively (see Table 2). A minor part of methane is found in CH_3OH environment, however, the detection at this level may be sensitive to e.g. baseline selection. Spectrum *c* is excluded from the analysis due to low signal-to-noise ratio. The $1.53''$ apertures display variations in ice composition with CH_4 in CO_2 to CH_4 in H_2O relative abundances decreasing towards the protostar. There is also an overall increase in column density towards the core, likely explained by an increase of density towards the center.

The presence of CH_4 in CO_2 matrix provides some insights on ice formation at early stages of the protostar. An interesting

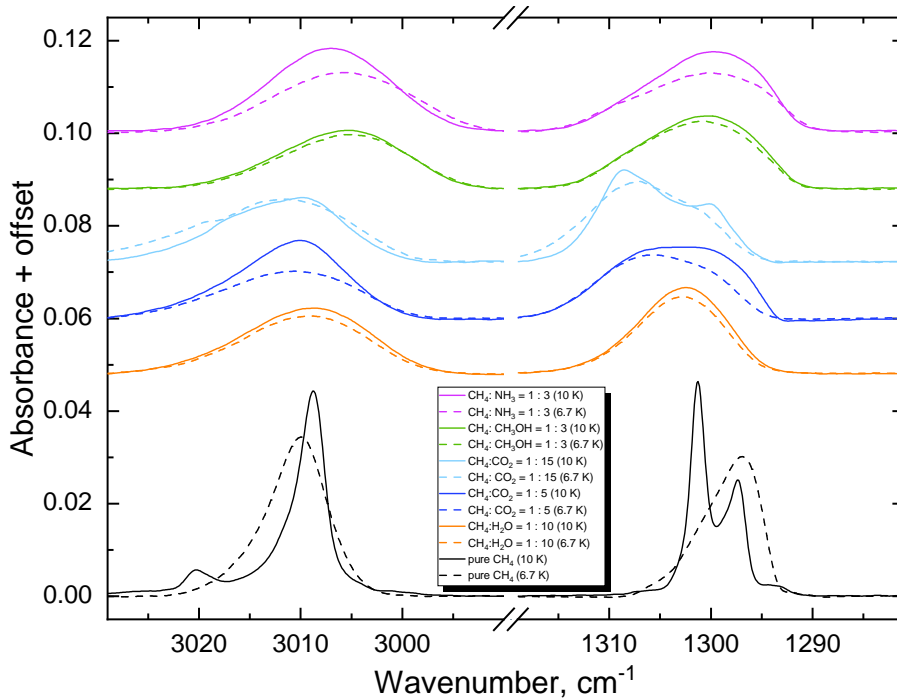


Fig. 1. The main vibrational modes of methane at 6.7 K and 10 K: the stretching mode at 3000 cm^{-1} ($3.33\text{ }\mu\text{m}$, ν_3) and the deformation mode at 1300 cm^{-1} ($7.7\text{ }\mu\text{m}$, ν_4), black is the pure methane, yellow is the $\text{CH}_4:\text{H}_2\text{O} = 1:10$ mixture, blue is the $\text{CH}_4:\text{CO}_2 = 1:5$ mixture, light blue is the $\text{CH}_4:\text{CO}_2 = 1:15$ mixture, green is the $\text{CH}_4:\text{CH}_3\text{OH} = 1:3$ mixture, purple is the $\text{CH}_4:\text{NH}_3 = 1:3$ mixture. Column density of CH_4 in all the IR spectra equals to $4.25 \times 10^{16}\text{ cm}^{-2}$.

Table 1: The position of the ν_3 and ν_4 methane modes in mixtures

Mixture	Component ratio	Temperature (K)	Peak position ν_3 (cm^{-1})	Peak position ν_4 (cm^{-1})	Band Strength ν_4 (cm^{-1})
CH_4	-	8	3010.0	1296.9	1.04×10^{-17a}
CH_4	-	10	3008.8	1301.3	8.4×10^{-18b}
			3020.5	1297.0	
$\text{CH}_4:\text{H}_2\text{O}$	1 : 10	6.7	3008.9	1302.7	8.8×10^{-18}
$\text{CH}_4:\text{H}_2\text{O}$	1 : 10	10	3008.6	1302.5	1.0×10^{-17}
$\text{CH}_4:\text{CO}_2$	1 : 5	6.7	3010.6	1305.6	9.3×10^{-18}
$\text{CH}_4:\text{CO}_2$	1 : 5	10	3010.1	1301.7	1.2×10^{-17}
$\text{CH}_4:\text{CO}_2$	1 : 15	6.7	3011.7	1307.0	1.0×10^{-17}
$\text{CH}_4:\text{CO}_2$	1 : 15	10	3009.8	1308.6	1.1×10^{-17}
			3039.9	1300.1	
$\text{CH}_4:\text{CH}_3\text{OH}$	1 : 3	6.7	3005.6	1300.8	1.0×10^{-17}
$\text{CH}_4:\text{CH}_3\text{OH}$	1 : 3	10	3005.2	1300.3	1.1×10^{-17}
$\text{CH}_4:\text{NH}_3$	1 : 3	6.7	3005.6	1300.2	1.0×10^{-17}
$\text{CH}_4:\text{NH}_3$	1 : 3	10	3007.0	1299.7	1.2×10^{-17}

Notes. ^(a) The band strength is taken from Gerakines & Hudson (2015b); ^(b) The band strength is taken from Bouilloud et al. (2015).

correlation is observed between CH_4 and CO_2 . The Spearman's ρ and p -values (Spearman 1904) for CO_2 and CH_4 column densities ($\rho = 0.9$, $p=0.007$) and abundances ($\rho = 0.9$, $p=0.003$) indicate strong, statistically significant, positive correlation between these species. The correlations between CH_4 and CO_2 are known from as early as Spitzer methane survey (Öberg et al. 2008). Modeling presented in Garrod & Pauly (2011) shows that under certain conditions methane and CO_2 can form concurrently, occupying the innermost layers of ice mantles. Ferrero et al. (2024) explored the reactivity of ${}^3\text{C-OH}_2$ complex with various species, revealing barrierless reactions with atomic O and H. These reactions lead to production of CH_2 and CO , which are the direct precursors to CH_4 and CO_2 , respectively. While parallel formation of methane and CO_2 is not largely explored, these results can be interpreted as evidence towards the concurrence for these processes.

4. Astrochemical implications and Conclusions

In this paper we present spectra of pure methane and binary mixtures with methane for 6.7 K and 10 K deposition temperatures.

The following mixtures are presented in this paper: $\text{CH}_4:\text{H}_2\text{O} = 1:10$, $\text{CH}_4:\text{CO}_2 = 1:5$, $\text{CH}_4:\text{CO}_2 = 1:15$, $\text{CH}_4:\text{CH}_3\text{OH} = 1:3$ and $\text{CH}_4:\text{NH}_3 = 1:3$. All spectra of methane in astrochemically relevant mixture ratios are presented for the first time at 6.7 K. The new band strength values and spectra obtained at temperature below 9 K reveal the following astrochemical implications:

1. Currently, the band strength of pure methane at 10 K is used majorly for column density estimations in observational data (e.g. McClure et al. 2023; Rocha et al. 2024, 2025). However, solid interstellar methane is found in mixtures with other icy species rather than in pure form. We also note that interstellar ices differ from laboratory analogues both in how they are produced and how they are processed. Thus, while the band strengths in Table 1 provide a better basis for interpreting obser-

Table 2: Aperture parameters and values derived from the fit

Aperture	Coordinates	$N(\text{CH}_4)$ [10^{17} cm^{-2}]	$\text{CH}_4:\text{H}_2\text{O}$ [%]	$\text{CH}_4:\text{CO}_2$ [%]	$\text{CH}_4:\text{CH}_3\text{OH}$ [%]	$N(\text{CO}_2)$ [10^{18} cm^{-2}]	$N(\text{H}_2\text{O})$ [10^{19} cm^{-2}]	$N(\text{CH}_4)/N(\text{H}_2\text{O})$ [%]
total	19:37:01.0868 +07:34:08.9309	5.0	64	32	4	2.8	1.2	4.3
a	19:37:01.1384 +07:34:10.3022	3.8	65	35	-	2.5	1.0	3.8
b	19:37:01.0348 +07:34:10.3022	5.6	70	30	-	3.1	1.2	4.8
c	19:37:01.1892 +07:34:08.9298	2.8	37	53	10	2.4	1.1	2.5
d	19:37:01.0868 +07:34:08.9309	4.1	52	34	14	2.2	1.2	3.4
e	19:37:00.9841 +07:34:08.9298	6.4	75	23	2	3.9	1.9	3.4
f	19:37:01.1375 +07:34:07.5764	4.1	74	26	-	2.4	1.3	3.1
g	19:37:01.0350 +07:34:07.5764	5.4	70	30	-	3.0	1.8	3.1

Notes. Apertures are listed following the notation in Fig. 2. Coordinates are given for the aperture centers in the form of R.A. and DEC. $N(\text{X})$ denotes column density of the species X. The columns denoted as $\text{CH}_4:\text{X}$ ($\text{X}=\text{H}_2\text{O}, \text{CO}_2, \text{CH}_3\text{OH}$) show the contribution of methane in $\text{CH}_4:\text{X}$ mixture to the total CH_4 column density listed in column 3. $N(\text{CH}_4)/N(\text{H}_2\text{O})$ is the CH_4 abundance relative to solid H_2O .

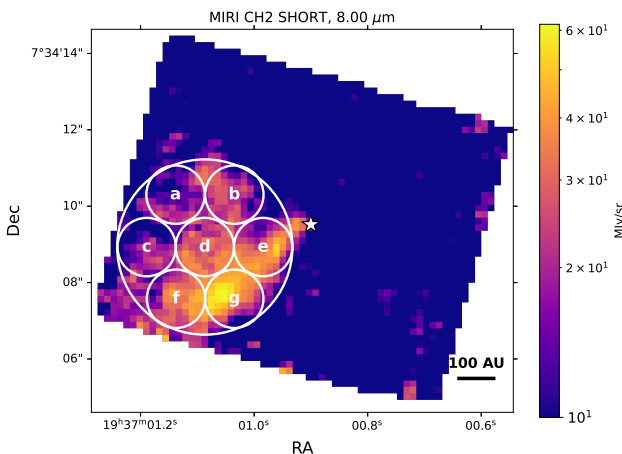


Fig. 2: B335 intensity map at $8 \mu\text{m}$ using the JWST MIRI-MRS spectrograph data. Small circles denote the $1.53''$ apertures, big circle denotes the $4.59''$ aperture. The center coordinates of chosen apertures are listed in Table 2.

vations, they are still approximate. Nevertheless, our new data invites a discussion on recent literature estimates. Since the ν_4 methane band strengths in mixtures are $\approx 20\%$ higher on average than the band strength of pure methane at 10 K , the column densities of interstellar methane may be overestimated by this value in e.g. McClure et al. (2023). Interestingly, this partially explains the underestimation of solid methane abundance by astrochemical models toward background stars NIR38 and J110621 reported in Jiménez-Serra et al. (2025).

2. We present the the first publicly available digital spectral library of methane absorbance spectra in non- H_2O environment, providing the possibility to identify non- H_2O methane environments on newly obtained JWST spectra. Solid methane is typically considered to reside in polar water-rich environment due its early formation along with water ice (see e.g. Hasegawa et al. 1992; Clément et al. 2023; Borschcheva et al.

2025). This is further supported by successful fits of methane features in JWST spectra of interstellar ices with $\text{CH}_4:\text{H}_2\text{O}$ mixtures (e.g. Chen et al. 2024; Rocha et al. 2024, 2025). However, there are possible evidences for its presence in mixtures with other molecules. For example, works by Boogert et al. (1996) and Nakibov et al. (2025) show that observed shapes of $7.7 \mu\text{m}$ methane feature can be partially interpreted with non- H_2O methane-containing mixtures. Additionally, icy methane mixed with apolar species such as N_2 and CO is found on icy bodies in the outer Solar system (e.g., Emtiaz et al. 2022). The obtained spectra of ices of astrochemical ratios are published on Zenodo (DOI: 10.5281/zenodo.15350566). Comparison between spectra obtained at 6.7 K and 10 K reveal temperature-induced changes in shape and peak position, although we find it unlikely that these differences are prominent enough to be discerned within the observational data. However, it is known that central regions of prestellar cores are well-shielded from external heating radiation. Consequently, as shown both observationally (Pagani et al. 2004, 2007; Crapsi et al. 2007; Pagani et al. 2015) and theoretically (Keto & Field 2005; Keto & Caselli 2010, and references therein), dust temperature there may reach 6 K . According to a recent modeling by Borschcheva et al. (2025), approximately 80% of solid methane in the prestellar core L1544 resides on grains with temperature below 9 K . Thus, to accurately interpret future observations of ices on a line of sight toward L1544, laboratory spectra and band strengths of mixtures obtained both at 6.7 K and 10 K might be needed. The presented spectra can be directly compared to observational data, because the ν_4 deformation mode of methane is unlikely to be affected by grain size, depending mostly on temperature and molecular environment (Boogert et al. 1997).

3. We present the first spatial survey performed on JWST MIRI-MRS data, exploring methane in B335. The results show that about 30% of solid methane is found in CO_2 environment, rather than in H_2O matrix. The consistency between findings in full and smaller apertures proves the usability of presented spectra for JWST data analysis. The observed ice composition gradient further highlights that JWST provides enough sensitivity for such studies, prompting further research.

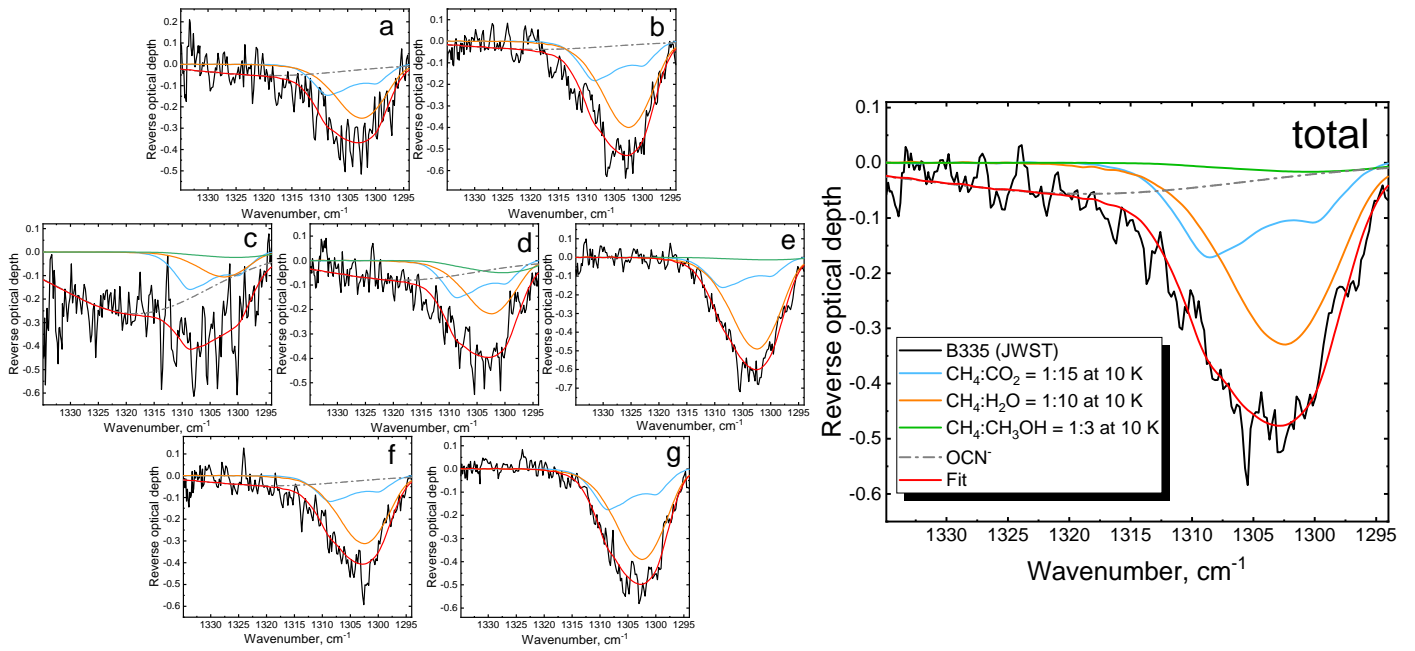


Fig. 3: Observational data fitted with ISEAge laboratory mixtures (solid lines). Orange color shows $\text{CH}_4:\text{H}_2\text{O} = 1:10$ mixture at 10 K, blue color — $\text{CH}_4:\text{CO}_2 = 1:15$ at 10 K, green color — $\text{CH}_4:\text{CH}_3\text{OH} = 1:3$ at 10 K, and OCN^- is presented in gray color. Final fit is presented in red color.

5. Data availability

The laboratory infrared absorbance spectra in transmission regime in the 2.5–15.9 μm (4000–630 cm^{-1}) region for CH_4 in different environments at 6.7 K and 10 K can be found on Zenodo at the following link: <https://zenodo.org/records/15350566>.

Acknowledgements. The authors thank Prof. Dr. Paola Caselli for the discussion on the dust temperature in prestellar cores, and Ms. Katerina Borshcheva for providing the information on the distribution of methane ice in the model of L1544. We thank the anonymous reviewer for their comments that helped us to improve the manuscript. This research work is funded by the Russian Science Foundation via 23-12-00315 agreement.

References

Abplanalp, M. J., Jones, B. M., & Kaiser, R. I. 2018, PCCP, 20, 5435
 Alsindi, W. Z., Gardner, D. O., van Dishoeck, E. F., & Fraser, H. J. 2003, CPL, 378, 178
 Baratta, G. A., Leto, G., & Palumbo, M. E. 2002, A&A, 384, 343
 Barman, T. S., Konopacky, Q. M., Macintosh, B., & Marois, C. 2015, ApJ, 804, 61
 Bergantini, A., Góbi, S., Abplanalp, M. J., & Kaiser, R. I. 2018, ApJ, 852, 70
 Bjerkeli, P., Ramsey, J. P., Harsono, D., et al. 2019, A&A, 631, A64
 Boogert, A. C. A., Gerakines, P. A., & Whittet, D. C. B. 2015, ARA&A, 53, 541
 Boogert, A. C. A., Helmich, F. P., van Dishoeck, E. F., et al. 1998, A&A, 336, 352
 Boogert, A. C. A., Schutte, W. A., Helmich, F. P., Tielens, A. G. G. M., & Wooden, D. H. 1997, A&A, 317, 929
 Boogert, A. C. A., Schutte, W. A., Tielens, A. G. G. M., et al. 1996, A&A, 315, L377
 Borshcheva, K., Fedoseev, G., Punanova, A. F., et al. 2025, ApJ, 990, 163
 Bouilloud, M., Fray, N., Bénilan, Y., et al. 2015, MNRAS, 451, 2145
 Bushouse, H., Eisenhamer, J., Dencheva, N., et al. 2024, JWST Calibration Pipeline
 Carder, J. T., Ochs, W., & Herbst, E. 2021, MNRAS, 508, 1526
 Chen, Y., Rocha, W. R. M., van Dishoeck, E. F., et al. 2024, A&A, 690, A205
 Clément, A., Taillard, A., Wakelam, V., et al. 2023, A&A, 675, A165
 Cleveland, W. S. 1979, JASA, 74, 829
 Collings, M. P., Anderson, M. A., Chen, R., et al. 2004, MNRAS, 354, 1133
 Colwell, J. H., Gill, E. K., & Morrison, J. A. 1962, J. Chem. Phys., 36, 2223
 Crapsi, A., Caselli, P., Walmsley, M. C., & Tafalla, M. 2007, A&A, 470, 221
 de Barros, A. L. F., Bordalo, V., Seperuelo Duarte, E., et al. 2011, A&A, 531, A160
 Ehrenfreund, P., Kerkhof, O., Schutte, W. A., et al. 1999, A&A, 350, 240
 Emtiaz, S. M., Toriello, F., He, J., & Vidali, G. 2020, JPCA, 124, 552
 Emtiaz, S. M., Toriello, F., He, J., & Vidali, G. 2022, JPCA, 126, 1973
 Evans, II, N. J., Rawlings, J. M. C., Shirley, Y. L., & Mundy, L. G. 2001, ApJ, 557, 193
 Evans, II, N. J., Yang, Y.-L., Green, J. D., et al. 2023, ApJ, 943, 90
 Ferrero, S., Ceccarelli, C., Ugliengo, P., Sodupe, M., & Rimola, A. 2024, ApJ, 960, 22
 Ferrero, S., Pantaleone, S., Ceccarelli, C., et al. 2023, ApJ, 944, 142
 Förstel, M., Bergantini, A., Maksyutenko, P., Góbi, S., & Kaiser, R. I. 2017, ApJ, 845, 83
 Gálffy, M. & Olofsson, G. 2007, A&A, 475, 281
 Garrod, R. T. & Pauly, T. 2011, ApJ, 735, 15
 Gautier, D., Bezard, B., Marten, A., et al. 1982, ApJ, 257, 901
 Gerakines, P. A. & Hudson, R. L. 2015a, ApJ, 808, L40
 Gerakines, P. A. & Hudson, R. L. 2015b, ApJ, 805, L20
 Gerakines, P. A. & Hudson, R. L. 2020, ApJ, 901, 52
 Gerakines, P. A., Schutte, W. A., & Ehrenfreund, P. 1996, A&A, 312, 289
 Gibb, E. L., Whittet, D. C. B., Boogert, A. C. A., & Tielens, A. G. G. M. 2004, ApJS, 151, 35
 Glass, J. B. & Hörst, S. M. 2025, AREPS, 53, 283
 Goto, M., Vasyunin, A. I., Giuliano, B. M., et al. 2021, A&A, 651, A53
 Greenfield, P. & Miller, T. 2016, A&C, 16, 41
 Harada, N. & Herbst, E. 2008, ApJ, 685, 272
 Hasegawa, T. I., Herbst, E., & Leung, C. M. 1992, ApJS, 82, 167
 Hassel, G. E., Herbst, E., & Garrod, R. T. 2008, ApJ, 681, 1385
 Hodys, R., Johnson, P. V., Stern, J. V., Goguen, J. D., & Kanik, I. 2009, Icarus, 200, 338
 Hudgins, D. M., Sandford, S. A., Allamandola, L. J., & Tielens, A. G. G. M. 1993, ApJS, 86, 713
 Hudson, R. L., Gerakines, P. A., & Loeffler, M. J. 2015, PCCP, 17, 12545
 Hudson, R. L. & Moore, M. H. 1999, Icar, 140, 451
 Islam, F., Baratta, G. A., & Palumbo, M. E. 2014, A&A, 561, A73
 Jiménez-Serra, I., Megías, A., Salaris, J., et al. 2025, A&A, 695, A247
 Kaiser, R. I., Maity, S., & Jones, B. M. 2014, PCCP, 16, 3399
 Keto, E. & Caselli, P. 2010, MNRAS, 402, 1625
 Keto, E. & Field, G. 2005, ApJ, 635, 1151
 Kobashi, K., Okada, K., & Yamamoto, T. 1977, J. Chem. Phys., 66, 5568
 Krasnopol'sky, V. A., Maillard, J. P., & Owen, T. C. 2004, Icarus, 172, 537
 Krissansen-Totton, J., Garland, R., Irwin, P., & Catling, D. C. 2018, AJ, 156, 114
 Krupskii, I. N., Prokhatilov, A. I., & Gasan, V. M. 1973, JETPL, 17, 605
 Lacy, J. H., Carr, J. S., Evans, II, N. J., et al. 1991, ApJ, 376, 556
 Lamberts, T., Fedoseev, G., van Hemert, M. C., et al. 2022, ApJ, 928, 48
 Lee, J.-E., Evans, N. J., Baek, G., et al. 2025, ApJ, 978, L3

Maity, S., Kaiser, R. I., & Jones, B. M. 2014, *ApJ*, 789, 36

McClure, M. K., Rocha, W. R. M., Pontoppidan, K. M., et al. 2023, *NatAs*, 7, 431

Megeath, T., Anglada, G., Atnagulov, P., et al. 2021, Investigating Protostellar Accretion Across the Mass Spectrum, JWST Proposal. Cycle 1, ID. #1802

Mifsud, D. V., Herczku, P., Sulik, B., et al. 2023, *Atoms*, 11, 19

Mizuno, Y., Kofu, M., & Yamamuro, O. 2016, *JPSJ*, 85, 124602

Mizuno, Y., Zhao, Y., Akiba, H., et al. 2022, *J. Chem. Phys.*, 156, 034503

Mulas, G., Baratta, G. A., Palumbo, M. E., & Strazzulla, G. 1998, *A&A*, 333, 1025

Nakibov, R., Karteyeva, V., Petrushkevich, I., et al. 2025, *ApJ*, 978, L46

Öberg, K. I., Boogert, A. C. A., Pontoppidan, K. M., et al. 2008, *ApJ*, 678, 1032

Ozhiganov, M., Medvedev, M., Karteyeva, V., et al. 2024, *ApJ*, 972, L10

Pagani, L., Bacmann, A., Cabrit, S., & Vastel, C. 2007, *A&A*, 467, 179

Pagani, L., Bacmann, A., Motte, F., et al. 2004, *A&A*, 417, 605

Pagani, L., Lefèvre, C., Juvela, M., Pelkonen, V. M., & Schuller, F. 2015, *A&A*, 574, L5

Pattle, K., Ward-Thompson, D., Kirk, J. M., et al. 2015, *MNRAS*, 450, 1094

Qasim, D., Fedoseev, G., Chuang, K. J., et al. 2020, *NatAs*, 4, 781

Reipurth, B., Heathcote, S., & Vrba, F. 1992, *A&A*, 256, 225

Rocha, W. R. M., McClure, M. K., Sturm, J. A., et al. 2025, *A&A*, 693, A288

Rocha, W. R. M., Pilling, S., de Barros, A. L. F., et al. 2017, *MNRAS*, 464, 754

Rocha, W. R. M., van Dishoeck, E. F., Ressler, M. E., et al. 2024, *A&A*, 683, A124

Schrauwen, J. G. M., Cuppen, H. M., Ioppolo, S., & Redlich, B. 2025, *JPCA*, 129, 6883, pMID: 40680293

Slavicinska, K., Rachid, M. G., Rocha, W. R. M., et al. 2023, *A&A*, 677, A13

Smith, Z. L., Dickinson, H. J., Fraser, H. J., et al. 2025, *NatAs*, 9, 883

Spearman, C. 1904, *The American Journal of Psychology*, 15, 72

Sullivan, K. K., Boamah, M. D., Shulenberger, K. E., et al. 2016, *MNRAS*, 460, 664

Swain, M. R., Tinetti, G., Vasisht, G., et al. 2009, *ApJ*, 704, 1616

Thompson, M. A., Krissansen-Totton, J., Wogan, N., Telus, M., & Fortney, J. J. 2022, *PNAS*, 119, e2117933119

van Gelder, M. L., Ressler, M. E., van Dishoeck, E. F., et al. 2024, *A&A*, 682, A78

Yang, Y.-L., Green, J. D., Pontoppidan, K. M., et al. 2022, *ApJ*, 941, L13

Yıldız, U. A., Kristensen, L. E., van Dishoeck, E. F., et al. 2015, *A&A*, 576, A109

Zhu, C., Turner, A. M., Abplanalp, M. J., & Kaiser, R. I. 2018, *ApJS*, 234, 15

Appendix A: pure CH₄

There are three phases of solid methane under vacuum conditions. The crystalline phase II is stable below 20.4 K and has the *fcc* lattice with eight sublattices: six of which have site symmetry D_{2d} and two — site symmetry O_h (Kobashi et al. 1977). It displays a double peak structure of both ν_3 (3009 cm⁻¹ and 3021 cm⁻¹) and ν_4 (1301 cm⁻¹ and 1298 cm⁻¹) features. This phase reversibly transitions into phase I above the first transition temperature of 20.4 K and has *fcc* lattice with a single freely rotating molecule. The ν_3 and ν_4 features are positioned at 3010 cm⁻¹ and 1299 cm⁻¹, respectively. Phase II* is observed if methane ice is obtained by vapor deposition below 10 K. It displays a degree of orientational disorder between phase I and phase II (Emtiaz et al. 2020). In this phase the absorption bands of methane are positioned near 3010 cm⁻¹ and 1297 cm⁻¹ (Gerakines & Hudson 2015b). Phase II* cannot be obtained by cooling methane ice from the triple point or from phase II ice. On warm-up phase II* ice undergoes irreversible transition to phase II. The second transition temperature depends on experimental conditions due to metastability and is observed below 10 K (Colwell et al. 1962; Krupskii et al. 1973; Emtiaz et al. 2020).

Despite the extensive research carried out on methane solid phases in infrared at low temperatures in recent decades (Kobashi et al. 1977; Hudgins et al. 1993; Boogert et al. 1997; Mulas et al. 1998; Gerakines & Hudson 2015b; Hudson et al. 2015; Emtiaz et al. 2020; Gerakines & Hudson 2020), there is still an ambiguity between published studies. In several works (Hudgins et al. 1993; Gerakines et al. 1996; Mulas et al. 1998; Alsindi et al. 2003; de Barros et al. 2011) methane is claimed to be in phase II, but the presented spectral features differ significantly from the theoretically derived shape (Kobashi et al. 1977). Gerakines & Hudson (2015b) addressed this discrepancy by providing spectra of ‘amorphous methane’, suggesting that the literature spectra in the works above display partial amorphous-to-crystalline transition, which was caused by the high deposition rates and experimental constraints of the setups used.

Gerakines & Hudson (2015b) report that the majority of their spectra were obtained in the 8–12 K range, but the spectra are referred to as obtained ‘at 10 K’ for simplicity throughout the text. Thus, it is not clear at what temperature exactly were published experiments carried out, a point that also applies to Hudson et al. (2015). This ambiguity is significant, because the 8–12 K range includes published methane second transition temperatures (Colwell et al. 1962; Krupskii et al. 1973). We attempted to obtain the spectrum at their Fig. 1(f) at precisely 10 K, but failed even using a lower deposition rate than stated in their paper. Therefore, prior to obtaining the set of methane-bearing mixtures at 10 K we decided to investigate the transition between phase II* and phase II. Under the deposition rate and duration of experiments described in the main text methane retained phase II* structure when deposited at 6.7 K throughout the whole deposition time. In contrast, for deposition at 10 K, the double peak structure characteristic of phase II started to form once ice reached certain column density, see Figure A.1. At a deposition rate of $5.9 \times 10^{12} \text{ cm}^{-2} \text{ s}^{-1}$ the transition started after 35 minutes, corresponding to a column density of $1.2 \times 10^{16} \text{ cm}^{-2}$. We also conducted depositions at rates twice as low and twice as high: $2.95 \times 10^{12} \text{ cm}^{-2} \text{ s}^{-1}$ and $1.18 \times 10^{13} \text{ cm}^{-2} \text{ s}^{-1}$. In all cases, on further deposition the double peak evolved through intermediate shapes, similar to those shown by Gerakines & Hudson (2015b), before fully converting to the phase II structure. The change in peak structure occurs at a critical value of $1.2 \times 10^{16} \text{ cm}^{-2}$. This equals approximately to 6 monolayers of pure methane ice on each side of the Ge substrate, given that single monolayer column density is $1 \times 10^{15} \text{ cm}^{-2}$.

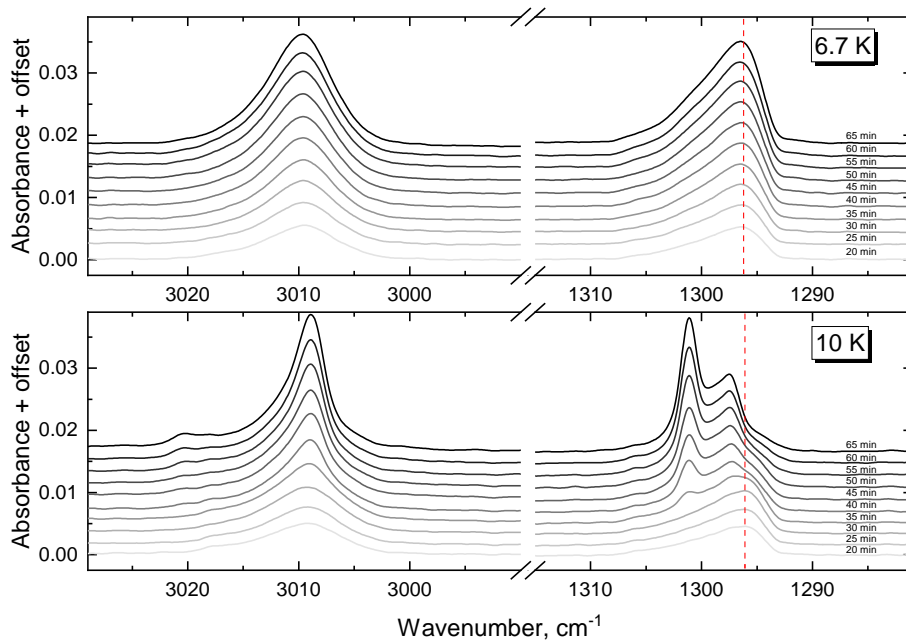


Fig. A.1. Top panel — selected IR spectra of pure methane deposition from 20th to 65th minutes with 6.7 K temperature (column density $(0.7 \text{ to } 2.3) \times 10^{16} \text{ cm}^{-2}$); bottom panel — IR spectra of pure methane deposition from 20th to 65th minutes with 10 K temperature (column density $(0.7 \text{ to } 2.3) \times 10^{16} \text{ cm}^{-2}$). The dashed red line shows the peak position of methane in phase II*.

From our experiments we conclude that phase II* is stable at 6.7 K. At 10 K phase II* is only observed in very thin methane films. In our experiments on Ge substrate, the maximum ice column density at which phase II* is still observed at 10 K is $1.2 \times 10^{16} \text{ cm}^{-2}$, independent of the deposition rate. Further ice growth at 10 K leads to the transition of phase II* to phase II through intermediate spectral shapes. While these intermediate spectra are similar to those mentioned in Gerakines & Hudson (2015b) we refrain from a more direct comparison. We expect that similar results can be obtained under minor differences in experimental conditions of other setups, which is expected given the environment-sensitive nature of metastable phase transition. A definitive answer would

come from X-ray diffractometry study as performed in [Mizuno et al. \(2016, 2022\)](#), which showed that other molecular ices that are ‘conventionally amorphous’ for astrochemistry can exhibit positionally ordered but orientationally disordered structure (CO or N₂), while other (CO₂, CS₂) are indeed amorphous.

We also note an instrumental effect that concerns both temperature programmed desorption (TPD) and static temperature experiments with volatile species. Here, we interpret the cases transparently reported by [Collings et al. \(2004\)](#) and [Schrauwen et al. \(2025\)](#). Methane temporarily adsorbs on warm surfaces (some cryostat parts, radiation shield, etc.) during the deposition and continuously releases even when the leak valves are closed, as in [Schrauwen et al. \(2025\)](#). The evacuation therefore is governed by the amount of temporarily stored methane rather than by turbomolecular pump’s efficiency, resulting in a ‘tail’ in QMS signal after deposition. During TPD warm surfaces release stored material early, polluting the QMS signal, as in [Collings et al. \(2004\)](#). Released gas can get readsorbed by the cold substrate. An example of that can be found in the cyclic experiment in [Gerakines & Hudson \(2015b\)](#) (see their Fig. 1, right column). We note that the integrated intensity increased after the first heating-holding-cooling cycle, indicating an increase in column density. Second cycle did not cause an increase as stored methane depleted on first heating. This increase did not affect the results of their paper.